Research Article | Vol. 26, No. 10 | 14 May 2018 | OPTICS EXPRESS 12707
Optics EXPRESS

# Analysis and correction of bias induced by phase stepping jitter in grating-based X-ray phase-contrast imaging

FABIO DE MARCO,[1,*] MATHIAS MARSCHNER,[1] LORENZ BIRNBACHER,[1] PETER NOËL,[1,2] JULIA HERZEN,[1] AND FRANZ PFEIFFER[1,2]

[1]*Technische Universität München, Department of Physics & School of BioMedical Engineering, James-Franck-Str. 1, 85748 Garching, Germany*
[2]*Technische Universität München, Klinikum rechts der Isar, Department of Diagnostic and Interventional Radiology, Ismaninger Str. 22, 81675 Munich, Germany*
[*]*fabio.de.marco@tum.de*

**Abstract:** Grating-based X-ray phase-contrast (gbPC) is an X-ray phase-contrast imaging method involving optical gratings that typically employs the Talbot self-imaging effect. X-ray phase contrast is known to provide significant benefits for biomedical imaging. To investigate these benefits for gbPC, a high-sensitivity gbPC micro-CT setup for small biological samples has been constructed. A gbPC projection measurement simultaneously retrieves the transmittance, differential-phase and dark-field modalities of a sample. Phase stepping, the most common gbPC acquisition technique, involves several acquisitions at different lateral positions of one of the gratings. The three modalities can then be retrieved by least-squares- or FFT-based methods.

Unfortunately, increasing differential-phase sensitivity also leads to an increased magnitude of artifacts introduced during retrieval of the modalities from the phase-stepping data, which limits image quality. Most importantly, processing of phase-stepping data with incorrect stepping positions (i.e., spatial sampling jitter) can introduce artifacts to the modalities. Using data from the high-sensitivity gbPC setup, as well as simulations, we show that an artifact is introduced by the jitter which is correlated with the phase of the stepping curve. We present a theoretical explanation for this correlation by introducing small deviations to an equidistant sampling of a stepping curve and approximating the effect on the calculation of the three gbPC modalities with a first-order Taylor approximation. Finally, we present an algorithm for the detection and removal of these artifacts that exploits these correlations. We show that this algorithm is able to eliminate these artifacts without degrading true image information.



**OCIS codes:** (340.7440) X-ray imaging; (110.0110) Imaging systems; (050.2770) Gratings; (050.5080) Phase shift; (340.7450) X-ray interferometry.

## References and links

1. A. Momose, "Recent Advances in X-ray Phase Imaging," Jpn. J. Appl. Phys. **44**, 6355–6367 (2005).
2. F. Pfeiffer, T. Weitkamp, O. Bunk, and C. David, "Phase retrieval and differential phase-contrast imaging with low-brilliance X-ray sources," Nat. Phys. **2**, 258–261 (2006).
3. A. Bravin, P. Coan, and P. Suortti, "X-ray phase-contrast imaging: from pre-clinical applications towards clinics," Phys. Med. Biol. **58**, R1–R35 (2013).
4. F. Pfeiffer, M. Bech, O. Bunk, P. Kraft, E. F. Eikenberry, C. Brönnimann, C. Grünzweig, and C. David, "Hard-X-ray dark-field imaging using a grating interferometer," Nat. Mater. **7**, 134–137 (2008).
5. M. Strobl, "General solution for quantitative dark-field contrast imaging with grating interferometers," Sci. Rep. **4**, 7243 (2014).
6. W. Yashiro, Y. Terui, K. Kawabata, and A. Momose, "On the origin of visibility contrast in x-ray Talbot interferometry," Opt. Express **18**, 16890–16901 (2010).
7. S. K. Lynch, V. Pai, J. Auxier, A. F. Stein, E. E. Bennett, C. K. Kemble, X. Xiao, W.-K. Lee, N. Y. Morgan, and H. H. Wen, "Interpretation of dark-field contrast and particle-size selectivity in grating interferometers," Appl. Opt. **50**, 4310–4319 (2011).

#321333 https://doi.org/10.1364/OE.26.012707
Journal © 2018 Received 7 Feb 2018; revised 15 Mar 2018; accepted 18 Mar 2018; published 3 May 2018

Optics EXPRESS


8. A. Momose, S. Kawamoto, I. Koyama, Y. Hamaishi, K. Takai, and Y. Suzuki, "Demonstration of X-Ray Talbot Interferometry," Jpn. J. Appl. Phys. **42**, L866–L868 (2003).
9. T. Weitkamp, A. Diaz, C. David, F. Pfeiffer, M. Stampanoni, P. Cloetens, and E. Ziegler, "X-ray phase imaging with a grating interferometer," Opt. Express **13**, 6296–6304 (2005).
10. A. Malecki, G. Potdevin, T. Biernath, E. Eggl, E. Grande Garcia, T. Baum, P. B. Noël, J. S. Bauer, and F. Pfeiffer, "Coherent Superposition in Grating-Based Directional Dark-Field Imaging," PLOS ONE **8**, e61218 (2013).
11. A. Malecki, G. Potdevin, T. Biernath, E. Eggl, K. Willer, T. Lasser, J. Maisenbacher, J. Gibmeier, A. Wanner, and F. Pfeiffer, "X-ray tensor tomography," EPL **105**, 38002 (2014).
12. M. Bech, O. Bunk, T. Donath, R. Feidenhans'l, C. David, and F. Pfeiffer, "Quantitative x-ray dark-field computed tomography," Phys. Med. Biol. **55**, 5529–5539 (2010).
13. L. Birnbacher, M. Willner, A. Velroyen, M. Marschner, A. Hipp, J. Meiser, F. Koch, T. Schröter, D. Kunka, J. Mohr, F. Pfeiffer, and J. Herzen, "Experimental Realisation of High-sensitivity Laboratory X-ray Grating-based Phase-contrast Computed Tomography," Sci. Rep. **6**, 24022 (2016).
14. H. Hetterich, M. Willner, S. Fill, J. Herzen, F. Bamberg, A. Hipp, U. Schüller, S. Adam-Neumair, S. Wirth, M. Reiser, F. Pfeiffer, and T. Saam, "Phase-contrast CT: qualitative and quantitative evaluation of atherosclerotic carotid artery plaque," Radiology **271**, 870–878 (2014).
15. S. Grandl, M. Willner, J. Herzen, A. Sztrókay-Gaul, D. Mayr, S. D. Auweter, A. Hipp, L. Birnbacher, M. Marschner, M. Chabior, M. Reiser, F. Pfeiffer, F. Bamberg, and K. Hellerhoff, "Visualizing typical features of breast fibroadenomas using phase-contrast CT: An ex-vivo study," PLOS ONE **9**, e97101 (2014).
16. A. A. Fingerle, M. Willner, J. Herzen, D. Münzel, D. Hahn, E. J. Rummeny, P. B. Noël, and F. Pfeiffer, "Simulated Cystic Renal Lesions: Quantitative X-ray Phase-Contrast CT – An in Vitro Phantom Study," Radiology **272**, 739–748 (2014).
17. Y. Zhang, X. Tian, and R. Liang, "Fringe-print-through error analysis and correction in snapshot phase-shifting interference microscope," Opt. Express **25**, 26554–26566 (2017).
18. F. Eng and F. Gustafsson, "Bias compensated least squares estimation of continuous time output error models in the case of stochastic sampling time jitter," IFAC Proc. Vol. **39**, 612–617 (2006).
19. T. Souders, D. Flach, C. Hagwood, and G. Yang, "The effects of timing jitter in sampling systems," in "6th IEEE Conference Record., Instrumentation and Measurement Technology Conference," (IEEE, 1989), pp. 199–203.
20. V. Revol, C. Kottler, R. Kaufmann, U. Straumann, and C. Urban, "Noise analysis of grating-based x-ray differential phase contrast imaging," Rev. Sci. Instrum. **81**, 073709 (2010).
21. G. W. Faris and R. L. Byer, "Three-dimensional beam-deflection optical tomography of a supersonic jet," Appl. Opt. **27**, 5202–5212 (1988).
22. F. Pfeiffer, O. Bunk, C. Kottler, and C. David, "Tomographic reconstruction of three-dimensional objects from hard X-ray differential phase contrast projection images," Nucl. Instrum. Methods Phys. Res. A **580**, 925–928 (2007).
23. Z. Wang and B. Han, "Advanced iterative algorithm for phase extraction of randomly phase-shifted interferograms," Opt. Lett. **29**, 1671–1673 (2004).
24. M. Marschner, M. Willner, G. Potdevin, A. Fehringer, P. B. Noël, F. Pfeiffer, and J. Herzen, "Helical X-ray phase-contrast computed tomography without phase stepping," Sci. Rep. **6**, 23953 (2016).
25. J. Vargas, J. A. Quiroga, and T. Belenguer, "Phase-shifting interferometry based on principal component analysis," Opt. Lett. **36**, 1326–1328 (2011).
26. G. Pelzer, J. Rieger, C. Hauke, F. Horn, T. Michel, M. Seifert, and G. Anton, "Reconstruction method for grating-based x-ray phase-contrast images without knowledge of the grating positions," J. Instrum. **10**, P12017 (2015).
27. J. Vargas, C. O. S. Sorzano, J. C. Estrada, and J. M. Carazo, "Generalization of the principal component analysis algorithm for interferometry," Opt. Commun. **286**, 130–134 (2013).
28. M. Seifert, S. Kaeppler, C. Hauke, F. Horn, G. Pelzer, J. Rieger, T. Michel, C. Riess, and G. Anton, "Optimisation of image reconstruction for phase-contrast x-ray Talbot-Lau imaging with regard to mechanical robustness," Phys. Med. Biol. **61**, 6441–6464 (2016).
29. H. Wen, H. Miao, E. E. Bennett, N. M. Adamo, and L. Chen, "Flexible Retrospective Phase Stepping in X-ray Scatter Correction and Phase Contrast Imaging Using Structured Illumination," PLOS ONE **8**, e78276 (2013).
30. S. Kaeppler, J. Rieger, G. Pelzer, F. Horn, T. Michel, A. Maier, G. Anton, and C. Riess, "Improved reconstruction of phase-stepping data for Talbot–Lau x-ray imaging," J. Med. Imaging **4**, 034005 (2017).
31. B. Münch, P. Trtik, F. Marone, and M. Stampanoni, "Stripe and ring artifact removal with combined wavelet—Fourier filtering," Opt. Express **17**, 8567–8591 (2009).

Optics EXPRESS

## 1. Introduction

### 1.1. Grating-based X-ray phase-contrast

Grating-based X-ray phase-contrast (gbPC) imaging has been shown to provide better soft-tissue contrast than regular attenuation-based imaging [1], while still working efficiently with conventional X-ray sources. [2, 3]. Three modalities can be retrieved from a single gbPC measurement: Besides *transmittance*, information about the angle of refraction is encoded in the *differential-phase* modality, and loss of visibility is encoded in the *dark-field* modality [4].

In gbPC, a Talbot interferometer is used to generate a periodic intensity pattern at certain positions downstream of a modulation grating ($G_1$). This is done by exploiting the Talbot effect, or, if a phase grating is used, the fractional Talbot effect [8]. Absorption, refraction and coherent scattering of X-rays by a sample have different effects on this periodic pattern: Absorption leads to uniform attenuation of the pattern, refraction affects its phase (i.e., the lateral shift), and small-angle scattering components orthogonal to both grating structures and beam direction causes a reduction in amplitude (see Fig. 1).

The primary cause of dark-field signal is small-angle scattering generated by electron density fluctuations on the micron scale, as exploited by (ultra-)small-angle X-ray scattering (USAXS/SAXS) experiments [5]. Besides sample thickness, dark-field signal strength depends on the autocorrelation function of the sample's electron density at the so-called correlation length, which is a function of X-ray energy and setup parameters. A detailed analysis of this relation can be found in [6, 7].

The resulting intensity patterns are typically too fine to be detected directly. Therefore, a transmission grating with the same period as the intensity pattern (the analyzer grating $G_2$) is introduced in front of the detector. This produces detectable moiré fringes due to a superposition of the periodic intensity pattern with the periodic $G_2$ transmittance function. By introducing a lateral displacement of one of the gratings, the phase of the moiré pattern is shifted. The observed intensity as a function of lateral displacement is typically sinusoidal. Amplitude, offset and phase of this sinusoidal function provide information about amplitude, offset and phase of the original intensity oscillations, and therefore about the amount of attenuation, refraction and small-angle scatter caused by the sample [4, 9].

Observation of this effect with a two-grating interferometer requires high transverse coherence of the X-ray source, prohibiting the use of standard X-ray tubes. However, the Talbot interferometer can be expanded to a Talbot-Lau interferometer by insertion of an attenuation grating (the source grating $G_0$) upstream of the modulation grating. This effectively separates the source spot into a periodic array of narrow, but mutually incoherent line sources. Each line source has sufficient transverse coherence to allow observation of the (fractional) Talbot effect, and the distance of adjacent line sources is matched so that the intensity modulations they produce at $G_2$ add up constructively [2].

To obtain a baseline reference, the above-mentioned phase-stepping procedure is performed twice: once with and once without a sample in the beam. The dependence of measured intensity on the lateral shift $x$ can be described as:

$$I^{\mathrm{s}}(x) = a_0^{\mathrm{s}} + a_1^{\mathrm{s}} \cos\left(x - \Phi_1^{\mathrm{s}}\right), \tag{1}$$

$$I^{\mathrm{f}}(x) = a_0^{\mathrm{f}} + a_1^{\mathrm{f}} \cos\left(x - \Phi_1^{\mathrm{f}}\right). \tag{2}$$

Here, $p$ denotes the analyzer grating period. The index s refers to the model parameters corresponding to the sample projection, the index f to those from the reference projection, the so-called *flat-field*. By lateral displacement of one of the three gratings, $I^{\mathrm{s}}$ and $I^{\mathrm{f}}$ are sampled at different values of lateral shift ($x = x_1, \ldots, x_N$). A fit of the model functions in Eq. (1) and (2) to the data can then be performed using least-squares- or FFT-based methods, which yields values for the curves' offsets $a_0^{\mathrm{s/f}}$, amplitudes $a_1^{\mathrm{s/f}}$, and phases $\Phi_1^{\mathrm{s/f}}$. Transmittance $T$, differential phase

Optics EXPRESS

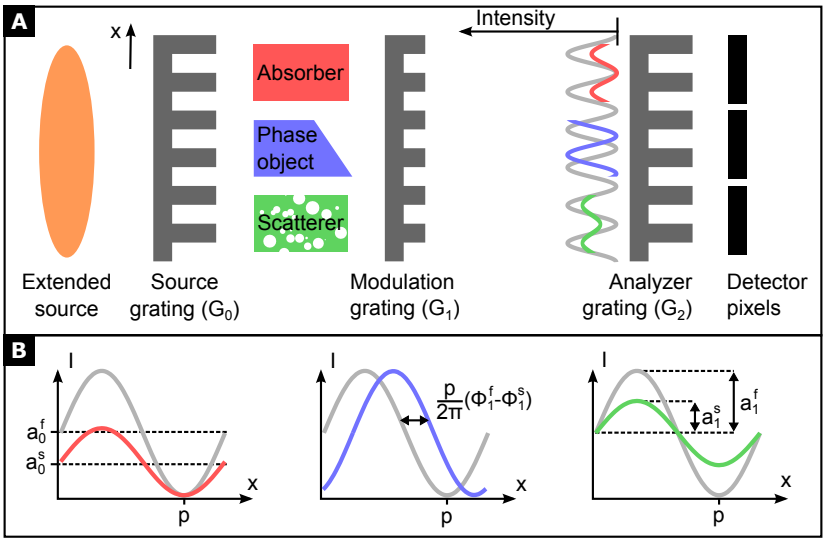


Fig. 1. (a): Effect of absorption, refraction and small-angle scattering on downstream intensity patterns in the Talbot-Lau interferometer. (b): The intensity patterns are resolved indirectly by recording the detector signals $I$ for different lateral shifts $x$ of either of the three gratings (of period $p$).

$\varphi$, and dark-field $D$ are then derived from these fit parameters via

$$T = \frac{a_0^{\mathrm{s}}}{a_0^{\mathrm{f}}},\ \varphi = \Phi_1^{\mathrm{s}} - \Phi_1^{\mathrm{f}},\ D = \frac{V^{\mathrm{s}}}{V^{\mathrm{f}}} = \frac{a_1^{\mathrm{s}}/a_0^{\mathrm{s}}}{a_1^{\mathrm{f}}/a_0^{\mathrm{f}}}. \tag{3}$$

For a CT scan, these modalities are acquired for many different projection angles, and three sets of volumetric data, namely attenuation coefficient $\mu$, refractive index decrement $\delta$, and linear diffusion coefficient $\varepsilon$, are reconstructed from sinograms of $T$, $\varphi$, and $D$, respectively.

In general, the directional dependence of the dark-field signal must be considered, and may be modeled e.g. as described in [10]. For X-ray dark-field CT, the situation is further complicated by the relative rotation of sample and beam direction. In X-ray tensor tomography, a three-dimensional scatter tensor can be retrieved for each voxel [11]. For a non-directional dark-field setup such as the one used here, the retrieved scalar volumetric quantity is an average over components of this tensor in many different directions (perpendicular to grating ridges and beam direction, for all tomographic angles). This reduction to a scalar quantity $\varepsilon$, as shown in [12], is however appropriate for the description of isotropic scatterers.

The high soft-tissue contrast of the refractive index decrement suggests future biomedical applications for gbPC-CT and other X-ray phase-contrast imaging methods [3].

### 1.2. High-sensitivity gbPC setup

The algorithm presented here was tested on data generated by the setup presented in [13]. This gbPC micro-CT setup with very high angular sensitivity was primarily used for the detectability of various pathologies via gbPC [14–16].

### 1.3. Observations and purpose

When processed with a simple FFT- or least-squares-based signal extraction algorithm, many gbPC-CT projections from the examined setup exhibit fringe-like artifacts. We found that the

Optics EXPRESS

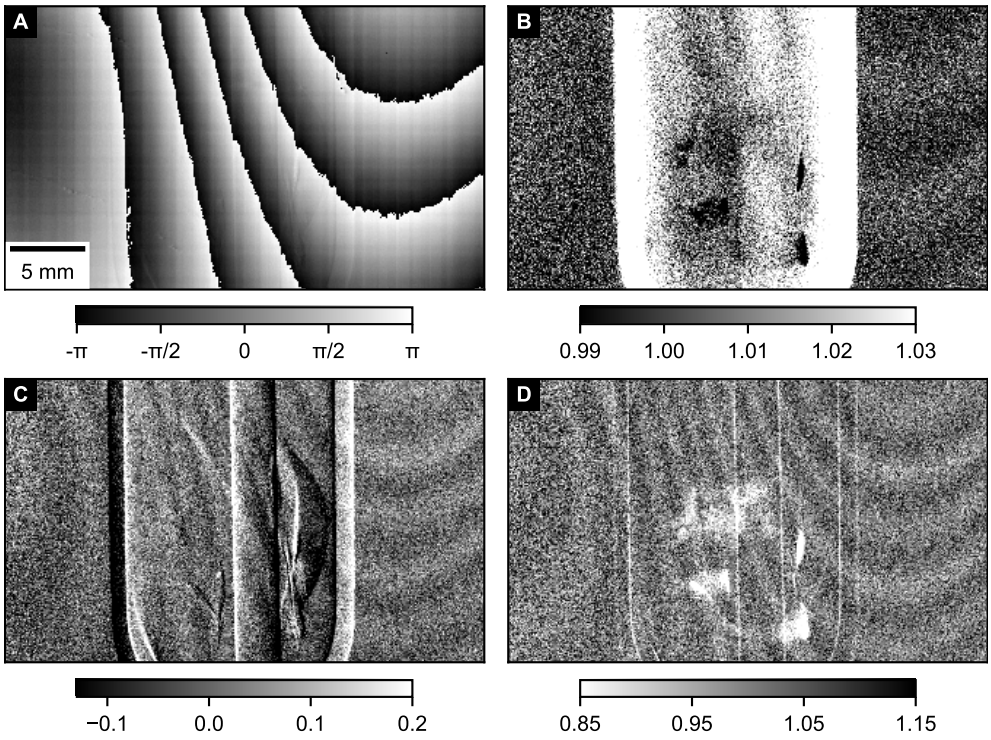


Fig. 2. Correlation of stepping curve phase $\Phi_1^s$ (a) and residual oscillations in projections of transmittance $T$ (b), differential-phase $\varphi$ (c) and dark-field $D$ (d) of a porcine cartilage sample in saline solution. A PMMA rod used for energy calibration is also visible. The phase-wrapping pattern in (a) correlates with the pattern of fringe artifacts in all three modalities. The artifacts in (c) and (d) evidently have twice the spatial frequency of the pattern in (b). Figs. 2(b)-2(d) were retrieved from a set of 11 phase-stepping images over one grating period (and another 11 flat-field phase-stepping images). Exposure time per image was 3 s. Acquisition was performed at the setup in [13], at 40 kVp (Mo anode) and a current of 70 mA.

spatial pattern of these artifacts correlates with that of the stepping curve phase of both the sample projection ($\Phi_1^s$) and the flat-field ($\Phi_1^f$). In visible-light phase-shifting interferometry (PSI), this type of artifact is known as the fringe-print-through (FPT) error [17]. In PSI, only the phase difference (i.e. differential phase) is commonly retrieved. We have observed these artifacts in all three gbPC modalities, but find that they are most prominent in the differential-phase and dark-field projection images. An example projection is shown in Fig. 2. The image of stepping curve phases in Fig. 2(a) is dominated by a high spatial gradient, which is mapped to the interval $[-\pi, \pi]$ since it is the argument (angle) of a complex value. Sample differential-phase information is only faintly visible.

The resulting phase-wrapping pattern shows a striking similarity to the artifacts present in the processed modalities [Figs. 2(b)-2(d)]. In the differential-phase and dark-field modalities, the artifact consists of two full oscillations per $2\pi$ range of $\Phi_1$ values, whereas in the transmittance image, only one oscillation appears in the same range.

In Sec. 2, it is shown that artifacts exhibiting this correlation can result from *jitter*, i.e. a discrepancy of the true sampling positions of the stepping curve and those implicitly assumed by the signal extraction algorithm. In Sec. 3, an algorithm for the removal (or reduction) of these

Optics EXPRESS

artifacts is presented, which exploits the observed correlations. An example of its application to measurement data is shown.

## 2. Calculation of fit coefficient errors due to jitter

### 2.1. Overview and prior art

In this section, the effect of a deviation of true and assumed stepping positions on the retrieved images is examined and we show that such deviations can cause a bias resembling the observed artifacts, as shown in Fig. 2. These deviations are commonly referred to as "jitter". Several methods have been developed to minimize the bias caused by jitter from a known or unknown random distribution [18,19]. However, these publications assume a single signal which is sampled a large number of times. The case of phase-stepping imaging, where many signals (i.e., pixels) are acquired simultaneously with the same jitter realization, can not be addressed with these methods. Additionally, the dependence of jitter-induced bias on the signal for any one particular realization of jitter values is not examined. In [20], Revol et al. provide variances of the relative error of the gbPC image modalities $T$, $\varphi$, and $D$ due to shot noise and phase-stepping jitter. However, the interpretation of jitter-related artifacts as "noise" obscures the fact that the artifacts have a non-random structure in any given noise realization.

In Sec. 2.2, jitter-induced biases in fit coefficients retrieved from a single stepping, namely $a_0$, $a_1$, and $\Phi_1$ from Eq. (1), (2) are estimated, and their dependence on a given jitter realization and the true value of $\Phi_1$ are examined. In Sec. 2.3, this is expanded to errors in the flat-field-corrected image modalities $T$, $D$, and $\varphi$ from Eq. (3), i.e. data retrieved from two sets of stepping data. The obtained results then serve as motivation for a correlation-based correction algorithm presented in Sec. 3. Finally, a statistical treatment of jitter is given in Sec. 2.4, where an approximate relationship between stepping uncertainty and error variances is presented.

We find that our results are in agreement with those from [20].

### 2.2. Correlation of single-stepping fit coefficients with stepping curve phase

In the following, we approximate a bias in the estimated values for the fit coefficients $a_0$, $a_1$, and $\Phi_1$ from Eq. (1), (2) when the sampling points of the stepping curve deviate from an equidistant placement over one period by small amounts. We find a correlation of the biases with $\sin(\Phi_1 - c)$ and $\sin(2\Phi_1 - c')$, in agreement with our observations from Sec. 1.3.

In the following, the *true* values of all variables are differentiated from their estimated values by the addition of the superscript "t". We assume sampling of a stepping curve at the positions $\vec{x}^{\,\mathrm{t}} = [x_1^{\mathrm{t}}, \ldots, x_n^{\mathrm{t}}]$. They are given in radians, consistent with Eq. (1), (2). Furthermore, we assume that these positions are close to an equidistant sampling $\vec{x} = [x_1, \ldots, x_n]$ over one stepping curve period (i.e. $x_k = 2\pi k/n$, $k = 1, \ldots, n$), and we define the deviation of each sampling position (i.e., the jitter) as $\xi_k \equiv x_k^{\mathrm{t}} - x_k$. This is a reasonable assumption since gbPC imaging setups are commonly programmed to sample stepping curves equidistantly, albeit with a positioning device of finite accuracy (which is reflected by the distribution of the $\xi_k$ values). The intensity values measured at the points $\vec{x}^{\,\mathrm{t}}$ are denoted $\vec{y}^{\,\mathrm{t}} = [y_1^{\mathrm{t}}, \ldots, y_n^{\mathrm{t}}]$. Image noise, i.e. random fluctuations of $\vec{y}^{\,\mathrm{t}}$, will be neglected for this calculation. The *true model* underlying the data is then given by

$$y_k^{\mathrm{t}} = a_0^{\mathrm{t}} + a_1^{\mathrm{t}} \cos\left(x_k^{\mathrm{t}} - \Phi_1^{\mathrm{t}}\right), \; k = 1, \ldots, n. \tag{4}$$

To retrieve estimates for $a_0^{\mathrm{t}}$, $a_1^{\mathrm{t}}$, and $\Phi_1^{\mathrm{t}}$ (denoted $a_0$, $a_1$ and $\Phi_1$), we fit a sinusoidal function to this data. In our model however, we assume an equidistant stepping, i.e. we incorrectly assume that the values $\vec{y}^{\,\mathrm{t}}$ were acquired at the equidistant sampling positions $\vec{x}$. These assumptions are illustrated in Fig. 3. Our signal extraction model is therefore:

$$y_k = a_0 + a_1 \cos\left(x_k - \Phi_1\right) = \beta_1 + \beta_2 \cos x_k + \beta_3 \sin x_k, \; k = 1, \ldots, n. \tag{5}$$

Optics EXPRESS

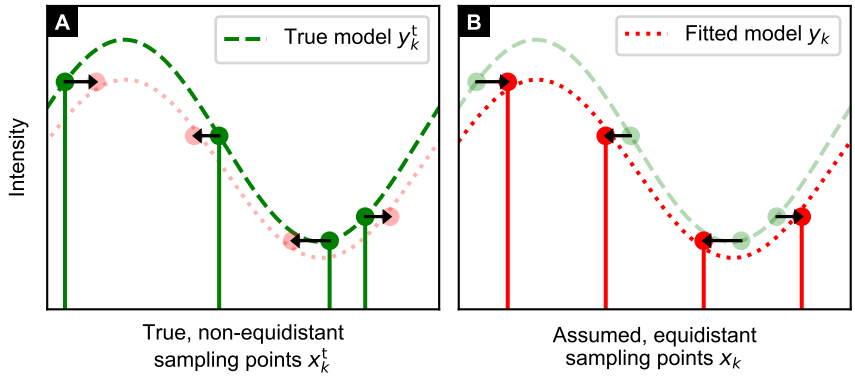


Fig. 3. Intensities are measured at sampling positions $x_k^t$ [abscissa in (a)], which, due to limited positioning accuracy, deviate from intended, equidistant stepping points $x_k$ [abscissa in (b)]. Misattribution of the measured values to the stepping points $x_k$ lead to a deviation between true and fitted curve parameters (dashed and dotted lines).

In Eq. (5), the model was converted to linear fit parameters, which are related to the original parameters via the following equations:

$$\beta_1 \equiv a_0, \tag{6}$$

$$\beta_2,\ \beta_3 \equiv a_1\cos(\Phi_1),\ a_1\sin(\Phi_1), \tag{7}$$

$$a_1,\ \Phi_1 \equiv \left(\beta_2^2+\beta_3^2\right)^{1/2},\ \arg(\beta_2+i\beta_3). \tag{8}$$

This linearization will simplify the calculation later on. To calculate the fit parameters, we can either use a discrete Fourier transform (DFT) or a least-squares minimization (both are equivalent for equidistant sampling). The least-squares solution is defined as

$$\beta_1,\beta_2,\beta_3 = \underset{\beta_1',\beta_2',\beta_3'}{\operatorname{argmin}} \sum_{k=1}^{n}\left[y_k(\beta_1',\beta_2',\beta_3') - y_k^t\right]^2. \tag{9}$$

We define the $j$-th coefficient of the DFT of $\vec{y}^{\,t}$ as

$$Y_j = \mathcal{F}\left\{\vec{y}^{\,t}\right\}_j = \frac{1}{n}\sum_{k=1}^{n}\exp(-2\pi ijk/n)y_k^t = \frac{1}{n}\sum_{k=1}^{n}\exp(-ijx_k)y_k^t. \tag{10}$$

Using this, the solution to Eq. (9) can be expressed as:

$$\beta_1 = Y_0 = \frac{1}{n}\sum_{k=1}^{n} y_k^t, \tag{11}$$

$$\beta_2 = 2\mathrm{Re}(Y_1) = \frac{2}{n}\sum_{k=1}^{n} y_k^t\cos x_k, \tag{12}$$

$$\beta_3 = -2\mathrm{Im}(Y_1) = \frac{2}{n}\sum_{k=1}^{n} y_k^t\sin x_k. \tag{13}$$

Optics EXPRESS

Inserting Eq. (4) for $y_k^{\mathrm{t}}$ in Eq. (11), (12), and (13) yields:

$$\beta_1(\vec{x}^{\,\mathrm{t}}) = \frac{1}{n}\sum_{k=1}^{n}\left[a_0^{\mathrm{t}} + a_1^{\mathrm{t}}\cos\left(x_k^{\mathrm{t}} - \Phi_1^{\mathrm{t}}\right)\right], \tag{14}$$

$$\beta_2(\vec{x}^{\,\mathrm{t}}) = \frac{2}{n}\sum_{k=1}^{n}\left[a_0^{\mathrm{t}} + a_1^{\mathrm{t}}\cos\left(x_k^{\mathrm{t}} - \Phi_1^{\mathrm{t}}\right)\right]\cos x_k, \tag{15}$$

$$\beta_3(\vec{x}^{\,\mathrm{t}}) = \frac{2}{n}\sum_{k=1}^{n}\left[a_0^{\mathrm{t}} + a_1^{\mathrm{t}}\cos\left(x_k^{\mathrm{t}} - \Phi_1^{\mathrm{t}}\right)\right]\sin x_k. \tag{16}$$

For equidistant stepping ($\vec{x}^{\,\mathrm{t}} = \vec{x}$), the error of all fit coefficients is zero ($\beta_j^{\mathrm{t}} = \beta_j$, and therefore $a_0^{\mathrm{t}} = a_0$, $a_1^{\mathrm{t}} = a_1$, $\Phi_1^{\mathrm{t}} = \Phi_1$). We assume that $\xi_k = x_k^{\mathrm{t}} - x_k$ is small for all $k$. Therefore, we approximate the error in all $\beta_j$ due to the incorrect sampling positions via a first-order Taylor series around the point $\vec{x}^{\,\mathrm{t}} = \vec{x}$:

$$\delta\beta_j = \beta_j(\vec{x}^{\,\mathrm{t}}) - \beta_j(\vec{x}) \tag{17}$$

$$\approx \sum_{k=1}^{n}\left.\frac{\partial\beta_j}{\partial x_k^{\mathrm{t}}}\right|_{\vec{x}^{\mathrm{t}}=\vec{x}}\underbrace{\left(x_k^{\mathrm{t}} - x_k\right)}_{=\xi_k} \tag{18}$$

A similar approach has previously been used for estimations of bias due to jitter, e.g. in [19]. Evaluation of Eq. (18) for $j = 1, 2, 3$ by using Eq. (14), (15), and (16) yields:

$$\delta\beta_1 \approx -\frac{a_1^{\mathrm{t}}}{n}\sum_{k=1}^{n}\xi_k\sin\left(x_k - \Phi_1^{\mathrm{t}}\right), \tag{19}$$

$$\delta\beta_2 \approx -\frac{2a_1^{\mathrm{t}}}{n}\sum_{k=1}^{n}\xi_k\sin\left(x_k - \Phi_1^{\mathrm{t}}\right)\cos x_k, \tag{20}$$

$$\delta\beta_3 \approx -\frac{2a_1^{\mathrm{t}}}{n}\sum_{k=1}^{n}\xi_k\sin\left(x_k - \Phi_1^{\mathrm{t}}\right)\sin x_k. \tag{21}$$

Since $a_0 = \beta_1$, the dependence of $\delta a_0$ on $\Phi_1^{\mathrm{t}}$ is already fully described by Eq. (19). To estimate the errors $\delta a_1$ and $\delta\Phi_1$, we can apply another first-order Taylor expansion, in equivalence to Eq. (18). Below, all partial derivatives are understood to be evaluated for $\vec{x}^{\,\mathrm{t}} = \vec{x}$, which is denoted by the subscript "$|_{\vec{x}}$":

$$\delta a_1 \approx \sum_{k=1}^{n}\left.\frac{\partial a_1}{\partial x_k^{\mathrm{t}}}\right|_{\vec{x}}\xi_k = \sum_{k=1}^{n}\left(\left.\frac{\partial a_1}{\partial\beta_2}\right|_{\vec{x}}\left.\frac{\partial\beta_2}{\partial x_k^{\mathrm{t}}}\right|_{\vec{x}} + \left.\frac{\partial a_1}{\partial\beta_3}\right|_{\vec{x}}\left.\frac{\partial\beta_3}{\partial x_k^{\mathrm{t}}}\right|_{\vec{x}}\right)\xi_k \tag{22}$$

$$= \left.\frac{\partial a_1}{\partial\beta_2}\right|_{\vec{x}}\sum_{k=1}^{n}\left.\frac{\partial\beta_2}{\partial x_k^{\mathrm{t}}}\right|_{\vec{x}}\xi_k + \left.\frac{\partial a_1}{\partial\beta_3}\right|_{\vec{x}}\sum_{k=1}^{n}\left.\frac{\partial\beta_3}{\partial x_k^{\mathrm{t}}}\right|_{\vec{x}}\xi_k \tag{23}$$

$$\overset{(18)}{\approx}\left.\frac{\partial a_1}{\partial\beta_2}\right|_{\vec{x}}\delta\beta_2 + \left.\frac{\partial a_1}{\partial\beta_3}\right|_{\vec{x}}\delta\beta_3. \tag{24}$$

An equivalent result can be obtained for $\delta\Phi_1$:

$$\delta\Phi_1 \approx \left.\frac{\partial\Phi_1}{\partial\beta_2}\right|_{\vec{x}}\delta\beta_2 + \left.\frac{\partial\Phi_1}{\partial\beta_3}\right|_{\vec{x}}\delta\beta_3. \tag{25}$$

Optics EXPRESS

Using Eq. (8), the derivatives of $a_1$ and $\Phi_1$ with respect to $\beta_2$ and $\beta_3$ are given as:

$$\frac{\partial a_1}{\partial \beta_2} = \frac{\beta_2}{(\beta_2^2+\beta_2^3)^{1/2}} = \frac{\beta_2}{a_1} = \cos\Phi_1, \qquad \frac{\partial a_1}{\partial \beta_3} = \frac{\beta_3}{(\beta_2^2+\beta_2^3)^{1/2}} = \frac{\beta_3}{a_1} = \sin\Phi_1, \tag{26}$$

$$\frac{\partial \Phi_1}{\partial \beta_2} = \frac{-\beta_3}{\beta_2^2+\beta_3^2} = \frac{-\beta_3}{a_1^2} = \frac{-\sin\Phi_1}{a_1}, \qquad \frac{\partial \Phi_1}{\partial \beta_3} = \frac{\beta_2}{\beta_2^2+\beta_3^2} = \frac{\beta_2}{a_1^2} = \frac{\cos\Phi_1}{a_1}. \tag{27}$$

When setting the true sampling positions $\vec{x}^{\,\mathrm{t}}$ equal to the equidistant sampling positions $\vec{x}$, the estimated fit coefficients are equal to their true values. Therefore:

$$\left.\frac{\partial a_1}{\partial \beta_2}\right|_{\vec{x}} = \cos\Phi_1^{\mathrm{t}}, \qquad \left.\frac{\partial a_1}{\partial \beta_3}\right|_{\vec{x}} = \sin\Phi_1^{\mathrm{t}}, \tag{28}$$

$$\left.\frac{\partial \Phi_1}{\partial \beta_2}\right|_{\vec{x}} = \frac{-\sin\Phi_1^{\mathrm{t}}}{a_1^{\mathrm{t}}}, \qquad \left.\frac{\partial \Phi_1}{\partial \beta_3}\right|_{\vec{x}} = \frac{\cos\Phi_1^{\mathrm{t}}}{a_1^{\mathrm{t}}}. \tag{29}$$

Inserting Eq. (20), (21), and (28) into Eq. (24) yields:

$$\begin{aligned}
\delta a_1 &\approx \cos\Phi_1^{\mathrm{t}} \times \frac{-2a_1^{\mathrm{t}}}{n}\sum_{k=1}^{n}\xi_k \sin(x_k-\Phi_1^{\mathrm{t}})\cos x_k + \sin\Phi_1^{\mathrm{t}} \times \frac{-2a_1^{\mathrm{t}}}{n}\sum_{k=1}^{n}\xi_k \sin(x_k-\Phi_1^{\mathrm{t}})\sin x_k \\
&= \frac{-2a_1^{\mathrm{t}}}{n}\sum_{k=1}^{n}\xi_k \sin(x_k-\Phi_1^{\mathrm{t}})(\cos\Phi_1^{\mathrm{t}}\cos x_k + \sin\Phi_1^{\mathrm{t}}\sin x_k) \\
&= \frac{-2a_1^{\mathrm{t}}}{n}\sum_{k=1}^{n}\xi_k \sin(x_k-\Phi_1^{\mathrm{t}})\cos(\Phi_1^{\mathrm{t}}-x_k) \\
\frac{\delta a_1}{a_1^{\mathrm{t}}} &\approx \frac{1}{n}\sum_{k=1}^{n}\xi_k \sin(2\Phi_1^{\mathrm{t}}-2x_k).
\end{aligned} \tag{30}$$

Likewise, plugging Eq. (29), (20), and (21) into Eq. (25) yields

$$\delta\Phi_1 = \frac{1}{n}\sum_{k=1}^{n}\xi_k\left[\cos(2\Phi_1^{\mathrm{t}}-2x_k)-1\right]. \tag{31}$$

Regardless of the values for $\xi_k$ or $x_k$, Eq. (19), (30), and (31) can always be expressed as simple sinusoidal dependencies on $\Phi_1^{\mathrm{t}}$ or $2\Phi_1^{\mathrm{t}}$, using the definition of complex amplitudes $\mathcal{A}_j$:

$$\frac{\delta a_0}{a_0^{\mathrm{t}}} \approx \frac{a_1^{\mathrm{t}}}{a_0^{\mathrm{t}}}\,\mathrm{Im}\left[\mathcal{A}_1\exp(i\Phi_1^{\mathrm{t}})\right] = \frac{a_1^{\mathrm{t}}}{a_0^{\mathrm{t}}}\,|\mathcal{A}_1|\sin\left(\Phi_1^{\mathrm{t}}+\arg\mathcal{A}_1\right), \tag{32}$$

$$\frac{\delta a_1}{a_1^{\mathrm{t}}} \approx \mathrm{Im}\left[\mathcal{A}_2\exp(2i\Phi_1^{\mathrm{t}})\right] = |\mathcal{A}_2|\sin\left(2\Phi_1^{\mathrm{t}}+\arg\mathcal{A}_2\right), \tag{33}$$

$$\delta\Phi_1 \approx \mathrm{Re}\left[\mathcal{A}_2\exp(2i\Phi_1^{\mathrm{t}})-\mathcal{A}_0\right] = |\mathcal{A}_2|\cos\left(2\Phi_1^{\mathrm{t}}+\arg\mathcal{A}_2\right)-\mathcal{A}_0, \tag{34}$$

$$\mathcal{A}_j = \frac{1}{n}\sum_{k=1}^{n}\xi_k\exp\left(-ijx_k\right) = \frac{1}{n}\sum_{k=1}^{n}\xi_k\exp\left(-2\pi ijk/n\right). \tag{35}$$

Comparing Eq. (35) and (10) shows that the arising complex amplitudes are simply components of the DFT of the vector $\vec{\xi}$ of all jitter values. This shows that within the scope of this calculation, $\vec{\xi}$ is sufficiently described by only three coefficients of its DFT. Note in particular that $\mathcal{A}_0$ in Eq. (34) is the mean of all elements of $\vec{\xi}$. A systematic offset of all sampling positions by the same value yields a nonzero value for $\mathcal{A}_0$ and therefore translates to an offset in the $\Phi_1$ estimate.

Optics EXPRESS

### 2.3. Dependence of the image modality errors on $\Phi_1^r$

The process described in Sec. 2.2 occurs in both sample scans and flat-field scans. The stepping jitter within these two acquisitions is typically not correlated and must therefore be described by two separate amplitudes $\mathcal{A}_{j,\mathrm{s}}$, $\mathcal{A}_{j,\mathrm{f}}$ ($j = 0, 1, 2$). The modalities are then calculated using Eq. (3), and the artifacts in $T$, $\varphi$, and $D$ as shown in Fig. 2 are hence each a combination of two artifacts, both being described by a separate complex amplitude. Since $\varphi = \Phi_1^{\mathrm{s}} - \Phi_1^{\mathrm{f}}$, it follows that

$$\delta\varphi = \delta\Phi_1^{\mathrm{s}} - \delta\Phi_1^{\mathrm{f}}. \tag{36}$$

$T$, $V$, and $D$ are results of a division of fit parameters. The error of these modalities can therefore not directly be expressed as a sinusoidal dependency on $\Phi_1$. However, assuming that the errors in $a_1$ and $a_0$ are small, they can again be estimated with a first-order approximation with respect to $a_1$ and $a_0$ around the point $(a_1^{\mathrm{t}}, a_0^{\mathrm{t}})$:

$$\delta T = \frac{a_0^{\mathrm{s,t}} + \delta a_0^{\mathrm{s}}}{a_0^{\mathrm{f,t}} + \delta a_0^{\mathrm{f}}} - \frac{a_0^{\mathrm{s}}}{a_0^{\mathrm{f}}} \quad \Rightarrow \frac{\delta T}{T^{\mathrm{t}}} \approx \frac{\delta a_0^{\mathrm{s}}}{a_0^{\mathrm{s,t}}} - \frac{\delta a_0^{\mathrm{f}}}{a_0^{\mathrm{f,t}}}, \tag{37}$$

$$\delta V = \frac{a_1^{\mathrm{t}} + \delta a_1}{a_0^{\mathrm{t}} + \delta a_0} - \frac{a_1^{\mathrm{t}}}{a_0^{\mathrm{t}}} \quad \Rightarrow \frac{\delta V}{V^{\mathrm{t}}} \approx \frac{\delta a_1}{a_1^{\mathrm{t}}} - \frac{\delta a_0}{a_0^{\mathrm{t}}}, \tag{38}$$

$$\delta D = \frac{V^{\mathrm{s,t}} + \delta V^{\mathrm{s}}}{V^{\mathrm{f,t}} + \delta V^{\mathrm{f}}} - \frac{V^{\mathrm{s,t}}}{V^{\mathrm{f,t}}} \quad \Rightarrow \frac{\delta D}{D^{\mathrm{t}}} \approx \frac{\delta V^{\mathrm{s}}}{V^{\mathrm{s,t}}} - \frac{\delta V^{\mathrm{f}}}{V^{\mathrm{f,t}}} \approx \frac{\delta a_1^{\mathrm{s}}}{a_1^{\mathrm{s,t}}} - \frac{\delta a_1^{\mathrm{f}}}{a_1^{\mathrm{f,t}}} + \frac{\delta a_0^{\mathrm{f}}}{a_0^{\mathrm{f,t}}} - \frac{\delta a_0^{\mathrm{s}}}{a_0^{\mathrm{s,t}}}. \tag{39}$$

Combining Eq. (32) and (33) with Eq. (36), (37), and (39), and assuming that $\varphi \ll 2\pi$, so that $\Phi_1^{\mathrm{s,t}} \approx \Phi_1^{\mathrm{f,t}} \equiv \Phi_1^{\mathrm{t}}$ leads to the results shown in Table 1.

Table 1. **Dependence of stepping-jitter-induced artifacts on stepping curve phase $\Phi_1^{\mathrm{t}}$ and complex amplitudes $\mathcal{A}_j$. These amplitudes are coefficients of the discrete Fourier transform of the jitter vector $\vec{\xi}$, see Eq. (35). A distinction between flat-field and sample phase-stepping is therefore necessary for $T$, $\varphi$, and $D$.**

| | |
|---|---|
| $\delta a_0/a_0^{\mathrm{t}}$ | $\approx V^{\mathrm{t}}\mathrm{Im}\left[\mathcal{A}_1 \exp(i\Phi_1^{\mathrm{t}})\right]$ |
| $\delta T/T^{\mathrm{t}}$ | $\approx \mathrm{Im}\left[(V^{\mathrm{s,t}}\mathcal{A}_1^{\mathrm{s}} - V^{\mathrm{f,t}}\mathcal{A}_1^{\mathrm{f}})\exp(i\Phi_1^{\mathrm{t}})\right]$ |
| $\delta\Phi_1$ | $\approx \mathrm{Re}\left[\mathcal{A}_2 \exp(2i\Phi_1^{\mathrm{t}})\right] - \mathcal{A}_0$ |
| $\delta\varphi_1$ | $\approx \mathrm{Re}\left[(\mathcal{A}_2^{\mathrm{s}} - \mathcal{A}_2^{\mathrm{f}})\exp(2i\Phi_1^{\mathrm{t}})\right] - (\mathcal{A}_0^{\mathrm{s}} - \mathcal{A}_0^{\mathrm{f}})$ |
| $\delta V/V^{\mathrm{t}}$ | $\approx \mathrm{Im}\left[\mathcal{A}_2 \exp(2i\Phi_1^{\mathrm{t}}) - V^{\mathrm{t}}\mathcal{A}_1 \exp(i\Phi_1^{\mathrm{t}})\right]$ |
| $\delta D/D^{\mathrm{t}}$ | $\approx \mathrm{Im}\left[(\mathcal{A}_2^{\mathrm{s}} - \mathcal{A}_2^{\mathrm{f}})\exp(2i\Phi_1^{\mathrm{t}}) + (V^{\mathrm{f,t}}\mathcal{A}_1^{\mathrm{f}} - V^{\mathrm{s,t}}\mathcal{A}_1^{\mathrm{s}})\exp(i\Phi_1^{\mathrm{t}})\right]$ |

Since $T$, $\varphi$, and $D$ are retrieved from two phase-stepping procedures (sample and flat-field measurement), jitter in both measurements may contribute to the artifacts, and is characterized by $\mathcal{A}_k^{\mathrm{s}}$ and $\mathcal{A}_k^{\mathrm{f}}$, respectively. Using these equations together with the definition for $\mathcal{A}_k$ in Eq. (35), shape and amplitude of artifacts can be approximately retrieved. For example, drawing $\xi_k$ values from a zero-mean normal distribution with standard deviation of 20% of the inter-step distance for an equidistant 7-step stepping yields good agreement between the results in Table 1 and ground truth in the majority of cases. The results from one such realization of $\vec{\xi}$ are shown in Fig. 4.

Due to the limited quantitative use of the above equations for artifact correction (as $\vec{\xi}$ is typically not known), we do not present an extensive analysis of their degree of accuracy. We believe that their value primarily lies in illustrating qualitatively the correlation with the stepping curve phase. In Sec. 3, we do however present an artifact correction algorithm based on these calculations, which is applicable even without knowledge of $\vec{\xi}$.

Optics EXPRESS

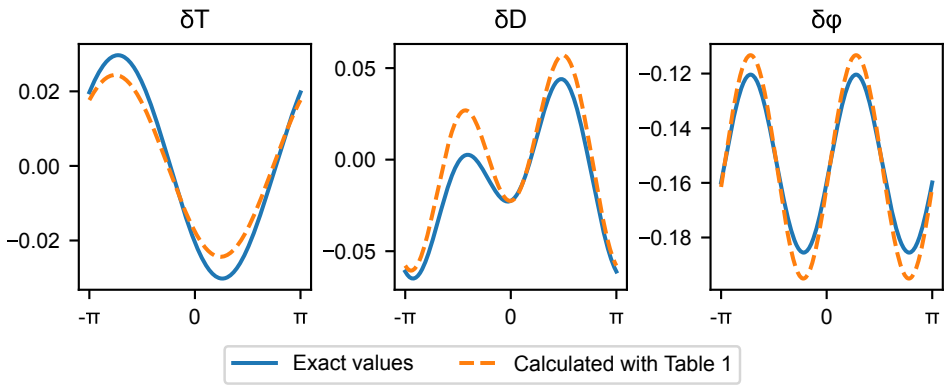


Fig. 4. Simulation of two non-equidistant stepping curves, followed by signal extraction with the assumption of equidistant sampling leads to errors in the three sample modalities, depending on the stepping curve phase (solid line). Knowing the exact stepping positions, the errors can be approximated with the results in Table 1. The step deviations $\xi_k$ were independently drawn from a normal distribution with mean zero and standard deviation $\sigma = 20\% \times 2\pi/n$, where $n = 7$ is the total number of steps. It was assumed that $V^{\mathrm{s,t}} = V^{\mathrm{f,t}}$.

### 2.4. *Relation of artifact magnitude to stepping accuracy*

The connection of stepping accuracy and artifact magnitude has previously been studied in [20]. In a similar approach, we assume that the error of the positioning device follows a normal distribution of mean 0 and standard deviation $\sigma_{\mathrm{mech}}$, and that errors of consecutive positioning steps are not correlated. The elements of $\vec{\xi}$ then also follow a zero-mean normal distribution, albeit with the standard deviation

$$\sigma = \sigma_{\mathrm{mech}} \frac{2\pi}{p_{\mathrm{G}}},$$

where $p_{\mathrm{G}}$ is the period of the stepped grating. It then follows from Eq. (35) that $\mathrm{Re}\,\mathcal{A}_j$ and $\mathrm{Im}\,\mathcal{A}_j$ are normally distributed with mean 0 and variance $\sigma^2/(2n)$, with zero covariance (for $j > 0$). $\mathcal{A}_0$ is real-valued with mean 0 and variance $\sigma^2/n$.

The distributions of the quantities in Table 1 can then be easily calculated: Considering that $\mathcal{A}_j$ is a bivariate Gaussian with zero mean and equal variances along the real and imaginary axis, it is rotationally invariant, which allows neglecting the complex exponentials $\exp(i\Phi_1^{\mathrm{t}})$, $\exp(2i\Phi_1^{\mathrm{t}})$. It follows that the terms enclosed in square brackets in Table 1 are also such bivariate Gaussians with mean zero and identical standard deviations along the real and imaginary axes. The standard deviations are given by the rule for summing (uncorrelated) normally distributed variables and are compiled in Table 2. The result is valid for any given value of $\Phi_1^{\mathrm{t}}$, and does not incorporate fluctuations due to a particular distribution of $\Phi_1^{\mathrm{t}}$ values.

The results for the flat-field-corrected quantities ($T$, $\varphi$, and $D$) are in agreement with those in [20], but equations for the quantities retrieved from a single phase-stepping ($a_0$, $V$, and $\Phi_1$) are not part of that publication. The "background case" described there refers to flat-field-corrected quantities in the absence of a sample. The equation for $\sigma(\delta\varphi)$ differs from its equivalent in [20] because the latter includes a prefactor of $1/(2\pi)$ in the definition of the differential-phase signal. This agreement therefore validates the calculations presented in Sec. 2.2 and 2.3.

For practical purposes, the ratio of positioning accuracy $\sigma_{\mathrm{mech}}$ and period of the stepped grating $p_{\mathrm{G}}$ ought to be selected such that the artifact amplitudes resulting from the equations in Table 2 are significantly smaller than the range of signals expected from the samples of interest. In the following section, we present a method for the detection and removal of these artifacts, based on their correlation with the stepping curve phases $\Phi_1$ (as given in Table 1).

Optics EXPRESS

Table 2. **Standard deviations of relative artifact amplitudes, in agreement with the values presented by Revol et al. in [20].**

| | |
|---|---|
| $\sigma(\delta a_0/a_0^{\mathrm{t}})$ | $= \pi\,(2/n)^{1/2}\,V^{\mathrm{t}}\,\sigma_{\mathrm{mech}}/p_{\mathrm{G}}$ |
| $\sigma(\delta T/T^{\mathrm{t}})$ | $= \pi\,(2/n)^{1/2}\,[(V^{\mathrm{s,t}})^2 + (V^{\mathrm{f,t}})^2]^{1/2}\,\sigma_{\mathrm{mech}}/p_{\mathrm{G}}$ |
| $\sigma(\delta\Phi_1)$ | $= \pi\,(6/n)^{1/2}\,\sigma_{\mathrm{mech}}/p_{\mathrm{G}}$ |
| $\sigma(\delta\varphi_1)$ | $= \pi\,(12/n)^{1/2}\,\sigma_{\mathrm{mech}}/p_{\mathrm{G}}$ |
| $\sigma(\delta V/V^{\mathrm{t}})$ | $= \pi\,(2/n)^{1/2}\,[1 + (V^{\mathrm{t}})^2]^{1/2}\,\sigma_{\mathrm{mech}}/p_{\mathrm{G}}$ |
| $\sigma(\delta D/D^{\mathrm{t}})$ | $= \pi\,(2/n)^{1/2}\,[2 + (V^{\mathrm{f,t}})^2 + (V^{\mathrm{s,t}})^2]^{1/2}\,\sigma_{\mathrm{mech}}/p_{\mathrm{G}}$ |

## 3. Algorithm for artifact removal

Since the amounts of stepping deviation $\vec{\xi}$ can often not be measured, the equations in Table 1 can not be solved explicitly for calculating artifacts in real data. However, the general shape of the correlations is independent of the particular values of $\vec{\xi}$. Variation of $\vec{\xi}$ merely affects amplitude and phase of this correlation (i.e., $\mathcal{A}_0$, $\mathcal{A}_1$, and $\mathcal{A}_2$). We therefore attempted to find approximations to the functions in Table 1 from the analysis of correlations between stepping curve phase $\Phi_1$ and the estimated modalities ($T$, $\varphi$, and $D$) in sample-free regions. Subsequent subtraction of the detected correlation from the images over the entire field of view then leads to a reduction in artifacts, ideally without compromising true image data.

### 3.1. Principle

A set of linearized model functions for stepping jitter artifacts, derived from Table 1, is introduced:

$$F\,[s_0, s_1, c_1, s_2, c_2; \Phi_1] = s_0 + s_1\sin(\Phi_1) + c_1\cos(\Phi_1) + s_2\sin(2\Phi_1) + c_2\cos(2\Phi_1) \tag{40}$$

Comparing Eq. (40) to Table 1, $s_1$ and $c_1$ represent $\mathcal{A}_1$, $s_2$ and $c_2$ represent $\mathcal{A}_2$, and $s_0$ represents $\mathcal{A}_0$. The set of all pixels with non-zero visibility in the projection image is denoted $R_0$. For a given projection from a gbPC setup, a sample-free, high-visibility subregion $R \subset R_0$ is identified. Within this region, a least-squares fit of $F$ to each of the modalities $T$, $\varphi$, and $D$ is performed (below: $X \in \{T, \varphi, D\}$), yielding an estimate for the correlation amplitudes and phases:

$$(\hat{s}_0^X, \hat{s}_1^X, \hat{c}_1^X, \hat{s}_2^X, \hat{c}_2^X) = \underset{s_0,s_1,c_1,s_2,c_2}{\operatorname{argmin}} \sum_{p\in R} \{F\,[s_0, s_1, c_1, s_2, c_2; \Phi_1(p)] - X(p)\}^2 \tag{41}$$

For $\Phi_1$, the stepping curve phase from either the sample projection or the flat-field may be used: Since $\varphi = \Phi_1^{\mathrm{s}} - \Phi_1^{\mathrm{f}} = 0$ in $R$, they should be identical. Subsequently, the determined correlation is subtracted from the entire image:

$$X_{\mathrm{corr}}(p) = X(p) - F\left[\hat{s}_0^X, \hat{s}_1^X, \hat{c}_1^X, \hat{s}_2^X, \hat{c}_2^X; \Phi_1(p)\right] + \hat{s}_0^X \;\forall p \in R_0 \tag{42}$$

In this step, an approximation is made that the artifact magnitude is independent of the true signal. Although incorrect, this approximation typically yields good results.

Note that, although the constant terms $\mathcal{A}_0^{\mathrm{s}}$ and $\mathcal{A}_0^{\mathrm{f}}$ do not occur for $\delta T/T^{\mathrm{t}}$ or $\delta D/D^{\mathrm{t}}$ in Table 1, inclusion of $\hat{s}_0^T$ and $\hat{s}_0^D$ *is* necessary for fit convergence: they describe the portions of the signal not correlated with $\Phi_1$, i.e. the mean "true" signal over the region $R$. Hence, they are not subtracted from the initial image in Eq. (42). For $\varphi$, offsets may have other sources beside stepping jitter, such as grating drifts. It may be determined after applying the above correction by subtracting its mean over the region $R$.

Optics EXPRESS

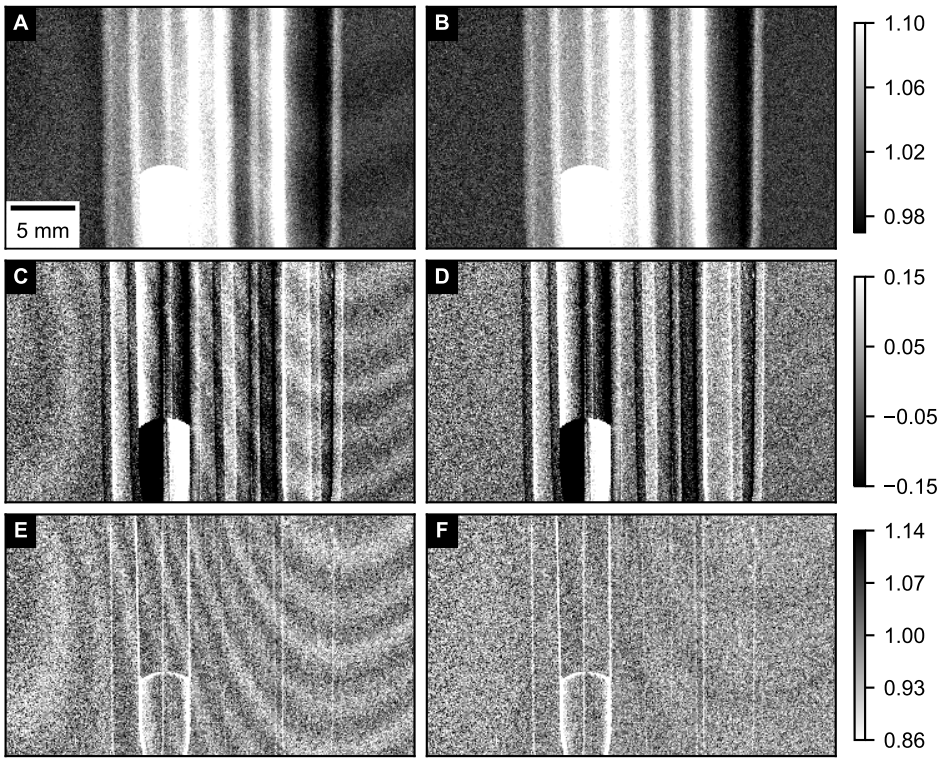


Fig. 5. Effect of the fringe artifact removal algorithm on projection modalities. Left and right columns: Before and after application of the correction. (a), (b): transmittance, (c), (d): differential-phase (values in radians), (e), (f): dark-field of an example projection. Narrow windowing was used to highlight artifacts. This is one of 801 projections comprising the gbPC-CT scan shown in Fig. 6.

Table 1 suggests that some fit coefficients should be set to zero ($s_1$ and $c_1$ for $\varphi$, $s_2$ and $c_2$ for $T$). However, correction of data from the setup described in Sec. 1.2 with different sets of active fit parameters revealed that activation of all fit coefficients appears to have no negative effects to correction quality. The veracity of the equations for $\delta\varphi$ and $\delta D/D^{\mathrm{t}}$ can be confirmed by fixing the important fit parameters to zero ($s_2$ and $c_2$ for $\varphi$, $s_1$ and $c_1$ for $T$), which results in incorrect treatment of stepping jitter artifacts, often leading to an *increase* in artifact amplitude.

### 3.2. Results

Figure 5 shows the effect of applying the algorithm to the transmittance ($T$), differential-phase ($\varphi$) and dark-field ($D$) modalities of one example projection from a gbPC micro-CT scan. The reduction in fringe artifact amplitude is immediately visible. Although not all projections of the associated CT scan feature such strong artifacts, artifact amplitude could be systematically reduced for nearly all projections in the scan. As can be seen in Fig. 6, reconstruction of differential-phase data treated with these algorithms yields a more homogeneous background in refractive index tomograms.

We have found that, if the sample-free region $R$ over which the fit is performed [cf. Eq. (41)] is chosen too small, random correlations between image noise (in $T$, $D$, and $\varphi$) and $\Phi_1$ will have a negative impact on the fit and the quality of the correction.

Optics EXPRESS

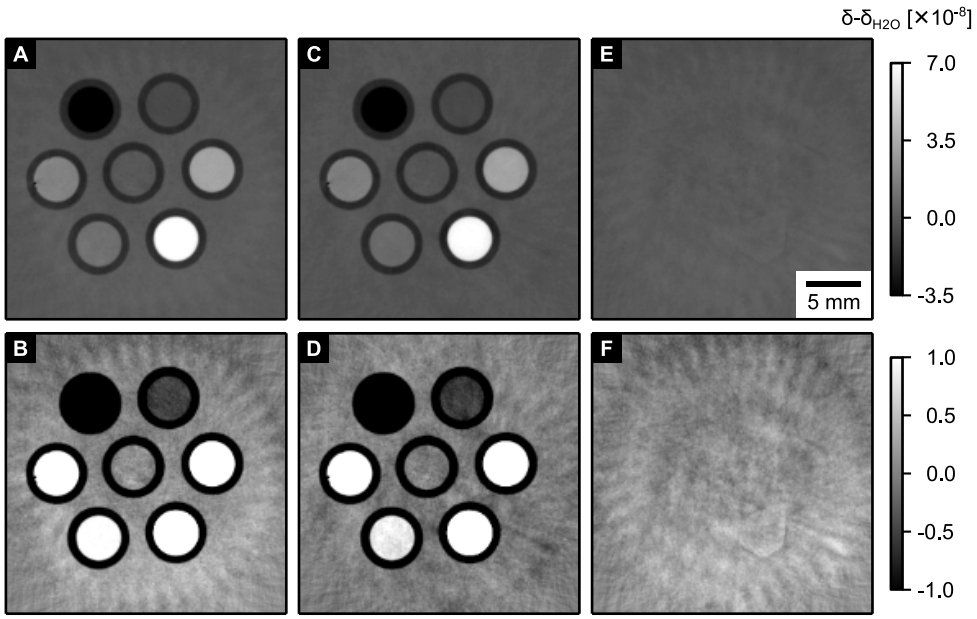


Fig. 6. Effect of the fringe artifact removal algorithm on tomograms of refractive index decrement $\delta$ of a liquid phantom submerged in a water bath [(a), (b): without correction, (c), (d): with correction, (e), (f): difference]. The phantom consists of seven plastic tubes containing different liquids (center: water, from bottom left clockwise: 5% / 10% NaCl in water; 25% / 50% / 75% / 100% glycerol in ethanol). The gbPC-CT scan consists of 801 phase-stepping projections, each composed of 11 individual phase-stepping images and an exposure time of 3 s per step. The acquisition was performed at the setup from [13], at 40 kVp (Mo anode) and a current of 70 mA. To show the image's dynamic range, but also highlight reconstruction artifacts, each image is shown with two different gray-value scales (top and bottom row). Simultaneous integration and filtered backprojection of differential-phase data was performed using an imaginary Hilbert filter [21, 22]. Since samples are immersed in a water bath, all flat-fields are acquired with the water bath in the beam. Therefore, the refractive index decrement $\delta$ is determined relative to water.

If a sufficiently large sample-free area is not available, it can be attempted to extend $R$ to sample-covered areas. If the sample's signal is sufficiently weak across a large range of $\Phi_1$ values, correct treatment of artifacts will often work, although care must be taken: The success depends on the severity of the artifacts (i.e., the magnitudes of $\mathcal{A}_1$ and $\mathcal{A}_2$), compared to the strength (and distribution) of the sample signal in $R$: High signal variations within $R$ effectively lead to "averaging" over variable correlation amplitudes and a decreased performance.

Furthermore, image noise affects the quality of detected correlation. If possible, increasing the size of $R$ ameliorates this problem. A comparison of the image before and after correction may help to decide whether or not to apply the algorithm in each case.

## 4. Discussion

The calculations presented in Sec. 2 examine a special case of parameter estimation bias induced by phase-stepping jitter, specifically dependence of the bias on the relative phase of the sampling points with respect to the sampled signal.

We calculated standard deviations of the artifacts and found them to be in agreement with the values previously reported in [20]. The treatment of phase-stepping jitter as a noise-like quantity

Optics EXPRESS

however obscures the fact that jitter-related artifacts are not really random in any given image, but appear as smooth features in the entire field of view. The random element is $\vec{\xi}$, which (along with the spatial distribution of the visibility $V$) defines the amplitude of the artifact in the whole image. We think that the description in Table 1 provides a clearer picture.

Concerning the algorithm presented in Sec. 3, a number of different methods for the correction of phase-stepping positions have previously been reported: In [23], Wang and Han introduced a method based on alternating least-squares minimizations for the retrieval of image signals and stepping positions for use in visible-light phase-shifting interferometry. An adaptation for gbPC imaging was given by Marschner et al. in [24]. This approach works independently of the shape of the moiré fringe pattern, but is iterative and may not converge for inaccurate starting values of step positions. It assumes global step positions, but could be extended to include a model for spatial dependence of step positions.

An alternative method also originating from visible-light interferometry was presented by Vargas et al. [25]. Using principle component analysis (PCA), all step positions can be retrieved in a single, fast computation step. It has been adapted for gbPC imaging by Pelzer et al. [26], but does not perform well for low numbers of moiré fringes and strongly attenuating samples. A combination of this method with the one given in [23] was presented in [27], which combines the applicability of PCA for arbitrary step positions with the high quality of results achieved with the method from [23]. It has been applied for gbPC phase-stepping data by Seifert et al. in [28].

A method based on the Fourier-transform method for the extraction of image signals was presented by Wen et al. [29]. The setup is adjusted to produce regular, high-frequency moiré fringes, and resultant higher harmonics of the Fourier-transformed images are analyzed to retrieve phase-stepping positions. Unlike the other methods, the retrieved phase-stepping positions even include spatial dependence, which is beneficial for electromagnetic phase-stepping. The method is non-iterative and therefore fast, but its applicability is limited in regions of low statistics.

Most recently, an approach has been presented by Kaeppler et al. [30], which first excludes phase-stepping images with very irregular step positions and then determines step positions on the remaining data by way of minimizing total variation in low-pass-filtered, normalized maps of visibility and mean flux. This is likely the most computation-intensive method and requires efficient nonlinear solvers. Furthermore, excluding measurement data from processing will inevitably increase noise levels.

Lastly, another option for correction is to apply de-striping algorithms such as the one presented in [31]. This method however requires horizontal or vertical stripes and therefore an according adjustment of moiré fringes. Since a "generic" filter does not take the image formation process into account, special care must be taken not to eliminate stripe-like sample features.

Compared to the above approaches, the method presented in Sec. 3 is easy to implement and requires little computing power. It benefits from an approximately equal distribution of all stepping curve phases over the full range $[-\pi, \pi]$ across the field of view, but the shape of the moiré fringes is not critical. It can only correct global step positions, which we believe is sufficient for ordinary (non-electronic) phase-stepping. Unlike the above methods, it is only accurate for small deviations from equidistant phase-stepping and can not retrieve true phase-stepping position values. However, sampling at *known* irregular step positions also contains a phase-dependent bias, which causes fringe-like artifacts very similar to the ones described in Sec. 2, and is not considered by the above-mentioned methods (possibly with the exception of [30]): Data processed with the method from [24] sometimes still contain visible fringe-like artifacts. Due to the similar shape of the two types of artifacts, the presented method however is able to remove both. Importantly, since the presented method operates on the processed gbPC modalities, it can also be used in addition to any of the other methods, e.g. where the first method was only partly able to eliminate the artifacts.

Optics EXPRESS

## 5. Conclusion

We presented observations of a correlation between image artifacts in all three gbPC projection modalities (transmittance, differential phase, dark-field) and stepping curve phase. We found that they can be explained by a deviation in true and assumed sampling positions (jitter) during phase stepping, and presented an approximate mathematical relationship between jitter values and bias amplitude for all three modalities, which is accurate for small jitter values. A simple and fast method for the correction of these artifacts, which is based on the determined correlations, was presented and demonstrated on experimental data.

Systematic investigations concerning the algorithm's performance for application to sample-covered areas should be performed. Additional improvements to the method could be attempted e.g. by incorporating the spatial variation of visibility, as well as a separate treatment of $\Phi_1^{s,t}$ and $\Phi_1^{f,t}$ for strongly phase-shifting samples. Furthermore, we think that the bias due to non-equidistant sampling at known positions deserves greater attention and should be evaluated in detail. The degree to which the presented algorithm is able to correct for this type of error should also be examined.

## Funding

European Research Council (ERC) (H2020, AdG 695045); DFG Gottfried Wilhelm Leibniz program.

## Acknowledgments

The authors wish to thank Sebastian Allner and Manuel Viermetz for their help and fruitful discussions. This work was carried out with the support of the Karlsruhe Nano Micro Facility (KNMF, www.kit.edu/knmf), a Helmholtz Research Infrastructure at Karlsruhe Institute of Technology (KIT). We acknowledge the support of the TUM Institute for Advanced Study, funded by the German Excellence Initiative.